Available online at www.sciencedirect.com
ScienceDirect
International Journal of Heat and Mass Transfer 51 (2008) 2686–2700
International Journal of HEAT and MASS TRANSFER
www.elsevier.com/locate/ijhmt

Loss of axisymmetry in the mixed convection, assisting flow past a heated sphere

Miroslav Kotouč *, Gilles Bouchet, Jan Dušek

Institut de Mécanique des Fluides et des Solides, UMR 7507 ULP/CNRS, 2 rue Boussingault, 67 000 Strasbourg, France

Received 19 March 2007; received in revised form 10 September 2007
Available online 3 December 2007

Abstract

For flows presenting linear instabilities, the laminar regime can be delimited accurately by the onset of the first bifurcation. For an unheated sphere, the primary bifurcation is preceded by a detachment of the boundary layer and a build up of a recirculation zone. In the mixed convection, the convection tends to prevent the boundary layer of the assisting flow from detaching and from a build up a recirculation zone. In this paper, the issue of the correlation between the boundary layer detachment and the loss of axisymmetry in the assisting flow is investigated with a special focus to the Prandtl number corresponding to flows in air ($Pr = 0.72$). For Richardson numbers up to 0.7, the detachment of the boundary layer (not necessarily a build up of the recirculation zone) is shown to be a precursor sign of a regular primary bifurcation similarly as for the wake of an unheated sphere. At this bifurcation, the flow stays steady but looses its axisymmetry. To assess the Prandtl number effects, the separation of the axisymmetric flow is investigated also in the $Pr = 7$ parameter plane and for Pr varying between 0.1 and 100 at fixed Reynolds and Richardson number values. The interest of the obtained results is twofold. Firstly, in the investigated parameter sub-domain, clear limits of the physical relevance of axisymmetric computations have been found. Within these limits, accurate values of the drag coefficients and overall Nusselt numbers are given. Secondly, in axisymmetric simulations, the detachment of the boundary layer may be a useful indication of the possible loss of axisymmetry.

Keywords: Mixed convection; Assisting flow; Flow separation; Loss of axisymmetry

1. Introduction

Mixed convection refers to flows driven both by buoyancy effects in a differentially heated fluid and an external flow. The mutual direction of the gravity and of the external flow is of particular importance for the flow dynamics and *assisting, opposing* and *cross flow* are distinguished in most studies. In the literature, significant attention has been paid to the investigation, mostly experimental, of the cross flow past a horizontal cylinder [1–3]. Numerical investigations of flows past a heated sphere take mostly advantage of the axisymmetry of the purely convective and of the assisting and opposing flows, characterized by an equal direction and, respectively, equal and opposed orientation of the external flow and of the buoyancy. The case of convection past a heated sphere has been recognized of special interest for understanding hydrodynamic and thermal effects present in many engineering processes such as vaporization of fuel droplets, combustion, condensation, drying, absorption, fusion of solid particles being transported in liquid medium, etc. The difficulty of a detailed experimental investigation of this system, namely that to access to the drag coefficient and the Nusselt number, has stimulated a significant number of numerical simulations described in the literature.

In the same way as for wakes, the parabolized equation approach may be valuable for investigating the boundary layers [4] and far plumes [5] but is unadapted for the characterization of the flow close to the rear stagnation point and thus cannot provide useful global characteristics such as the drag and the Nusselt number. The first to solve

* Corresponding author. Tel.: +33 390 242 896; fax: +33 388614300.
E-mail address: kotouc@imfs.u-strasbg.fr (M. Kotouč).

0017-9310/$ - see front matter © 2007 Elsevier Ltd. All rights reserved.
doi:10.1016/j.ijheatmasstransfer.2007.10.005

Nomenclature

C_D	drag coefficient ($C_D = F_D/\frac{1}{2}\rho v_\infty^2 \frac{\pi d^2}{4}$)
$C_D^{(c)}$	drag coefficient due to the pure forced convection
$C_D^{(f)}$	drag coefficient due to the pure free convection
C_D^{Dud}	drag coefficient defined by Dudek et al. ($C_D^{Dud} = F_D/\rho v^2$)
C_D^{Jia}	drag coefficient defined by Jia and Gogos ($C_D^{Jia} = F_D/\frac{1}{2}\rho v_{char}^2 \frac{\pi d^2}{4}$)
c_p	specific heat capacity
d	sphere diameter
F_D	drag force
$\mathbf{g}$	gravitational acceleration vector
Gr	Grashof number ($\beta g(T_S - T_\infty)d^3/v^2$)
L_{in}	inlet size of the computational domain
L_{out}	outlet size of the computational domain
L_{rad}	sidewise size of the computational domain
Nu	Nusselt number ($Nu = \alpha d/\lambda$)
Nu_{loc}	local Nusselt number
p	pressure
Pr	Prandtl number (v/κ)
$\dot{Q}$	heat flux
$\dot{Q}_{cond}$	pure conductive heat flux (calculated)
$\dot{Q}_{cond,th}$	pure conductive heat flux (theoretical)
r	distance from the flow axis
R	sphere radius
Re	Reynolds number ($v_{char}d/v$)
Re_c	critical Reynolds number for the onset of recirculation at the flow axis
Re_{crit}	critical Reynolds number for the regular bifurcation threshold
Re_r	critical Reynolds number for the separated flow to reach the flow axis
Re_s	critical Reynolds number for the onset of separation off the flow axis
Ri	Richardson number (Gr/Re^2)
s	spherical radial coordinate
t	time
T	temperature
$\mathbf{v}$	velocity vector
v	velocity
v_{char}	characteristic velocity
x	axial coordinate

Greek symbols

α	heat transfer coefficient
β	thermal expansion coefficient
Φ_d	angle of the boundary layer separation measured from the front stagnation point
Φ_r	angle of the boundary layer reattachment
κ	thermal diffusivity
λ	thermal conductivity
v	cinematic viscosity
θ	spherical angular coordinate
ρ	fluid density

Subscripts

θ	tangential direction
r	direction perpendicular to the flow axis
S	at sphere surface
x	axial direction
∞	at infinite distance from the sphere

Superscripts

*	non-dimensionalizeds

numerically the steady-state Navier–Stokes equations for the case of free convection were Geoola and Cornish [6]. They presented values of drag coefficient and Nusselt number for Grashof numbers $0.05 \leqslant Gr \leqslant 50$ (Gr based on the sphere radius R: $Gr = \beta g(T_S - T_\infty)R^3/v^2$). In a later paper [7], they presented transient results of Nu and C_D up to $Gr = 12{,}500$ for $Pr = 0.72$, 10 and 100. Dudek et al. [8] presented both experimental and numerical results for small Grashof numbers, $4 \times 10^{-4} \leqslant Gr \leqslant 0.5$ and $Pr = 0.72$ (with the same definition of Gr as Geoola and Cornish). Jia and Gogos [9] carried out the study for a wide range of radius based Grashof numbers ($10^1 \leqslant Gr \leqslant 10^8$) and for $Pr = 0.72$ and 7.

The earliest analytical studies on the combined effect of free and forced convection in the configuration of assisting flow are the works of Acrivos [10] (boundary–layer approximation) and of Hieber and Gebhart [11] (matched asymptotic expansion, Gr and Re being small). First experiments were carried out by Klyachko [12] and Yuge [13]. For recent experiments with very small particles, an electrodynamic chamber was used, see [14–18]. The published numerical results on convection past a sphere are all axisymmetric. The first to investigate numerically the assisting flow past a spherical particle (by a finite difference method) were Chen and Mucoglu [19]. In their work, they studied the surface heat transfer and the wall shear on a sphere with constant surface temperature for large Grashof and Reynolds numbers and the Richardson number ($Ri = Gr/Re^2$) ranging from ∞ (free convection) to 0 (pure forced convection) in the boundary layer approximation. The considered Prandtl number was 0.72. In their later work [20] they presented the same study for a sphere with a uniform heat flux. Wong et al. [21] solved the full Navier–Stokes and energy equation of an isothermal sphere in combined convection by a finite element method. Nguyen et al. [22] added two new features to the results of previous works – the transient effects and both internal and external thermal resistances (conjugate problem). Nazar et al. [23] carried out a very similar study

to that of [19] for two values of Prandtl number 0.7 and 6.8. Mograbi and Bar-Ziv [18] investigated, both experimentally and numerically, the dynamics of a spherical particle in mixed convection for small Grashof and Reynolds numbers and, in another paper [24], proposed an approximate expression for the drag.

The mixed convection in the configuration of opposing flow has been the topic of investigations presented, for example, in [15,17–20,22,23]. The dynamics of the opposing flow appears to be more complex and more difficult to simulate than that of assisting flow and will be treated elsewhere.

The present paper raises the question of the relevance of axisymmetric simulations of assisting flows. This problem has been thoroughly investigated for a non-heated sphere both numerically and experimentally [25–28]. It appears that the wake of a non-heated sphere undergoes a primary regular bifurcation at the Reynolds number (based on the sphere diameter) of 212. The flow becomes non-axisymmetric but remains steady until $Re \approx 275$ [27,28] when a secondary Hopf bifurcation sets in. Later on (at $Re = 500$), the wake was reported to be chaotic [29]. This complex dynamics can be simulated only in fully three-dimensional calculations and the instabilities completely modify both the flow pattern and the hydrodynamic forces acting on the sphere. As a result, in this case, axisymmetric simulations are physically valuable only until the onset of the axisymmetry breaking.

In this paper, we focus basically to the limits of the axisymmetric regime of an assisting flow. The problem is formulated mathematically in Section 2. The mathematical formulation of the thermal effects is limited to the Boussinesq approximation. All the numerical papers cited above are based on this approximation. Nevertheless, in practical applications, caution is required when deciding whether this approximation is still applicable. It is widely accepted that, in the air and water under normal laboratory conditions, the Boussinesq approximation is applicable for a thermal amplitude not exceeding several degrees. In [30, p. 15], the acceptable temperature difference for the Boussinesq approximation in the air and water is given, respectively, as 15 and 2 K. In [31] a 10% accuracy is guaranteed in fluid systems of laboratory size at 15 °C and atmospheric pressure for temperature variations of less than 1.25° in water and 28.6° in the air. Practically this means, in the framework of the present paper, that very small and thus, for the same Richardson number, significantly heated spheres are not covered by the scope of the approximation. Nonetheless, the Boussinesq approximation represents reasonable laboratory conditions for experiments on the transition to turbulence in air and water. E.g., a specific configuration of a sphere of diameter 11 cm brought to a 8° higher temperature than the surrounding air and placed in a flow of velocity 0.2 m/s is characterized by a Reynolds number of ≈1500 and a Richardson number of ≈0.7 corresponding to the extreme regimes investigated in this paper.

The used numerical method obtained by adjoining the temperature equation and the buoyancy term to the method described in [28] is presented briefly in Section 3. In the absence of thermal effects the numerical method has been successfully validated in many situations [32–34]. The simulation of heat and buoyancy effects is validated in the case of a free convection by comparison to a large amount of available data in Section 4. The main results are presented in Sections 5–7. The build up a recirculation zone is largely accepted to be a precursor sign of instabilities in wakes (see [35] for the case of an unheated cylinder, [36] for an assisting flow past a heated cylinder or [37] for the unheated sphere). Our method of investigation follows the usual logic of investigation of transitional flows consisting in increasing progressively the Reynolds and (in the present case also) the Richardson number to proceed from simpler to more complex regimes. As a consequence, we first investigate the precursor signs of instability before tackling the instability itself. As a result, Section 5, presented first and dealing with the Prandtl number $Pr = 0.72$ (for which the largest amount of bibliographic data is available) focuses on the detachment of the boundary layer and on the formation of the recirculation zone. Section 6 partly extends the results of Section 5 to other Prandtl numbers, namely to $Pr = 7$. The drag coefficients and Nusselt numbers are also given. Finally, Section 7 presents the results of the linear stability analysis of the flows undergoing a primary, axisymmetry breaking, bifurcation. The conclusions are drawn in Section 8.

2. Problem formulation

Our numerical simulations represent a hot sphere with a constant surface temperature immersed in a cold incompressible fluid. For the problem description and coordinate system definition see Fig. 1. This situation is mathematically described by a system of Navier–Stokes equations coupled with the energy equation (see for example [9]) for the unsteady flow of an incompressible fluid with constant properties. As stated in the introduction, the buoyancy effects are characterized by the Boussinesq approximation. The fluid properties are the density ρ, kinematic viscosity ν, thermal conductivity λ, specific heat at constant pressure c_p and the coefficient of thermal expansion β. The equations are non-dimensionalized using the following scaling: the sphere diameter d as a length scale, $v_{\mathrm{char}} = v_\infty$, the free

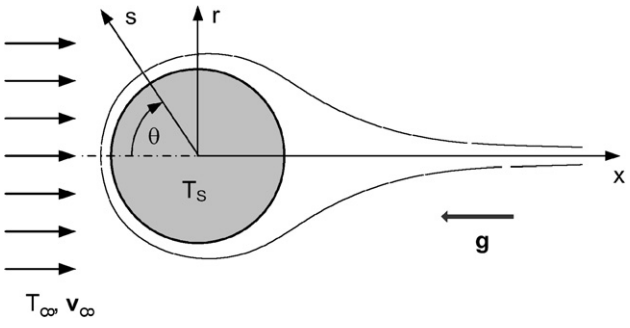

Fig. 1. Problem description and coordinate system.

stream velocity in an assisting flow (or $v_{\text{char}} = \sqrt{\beta g(T_S - T_\infty)d}$ in the case of free convection) as velocity scale, d/v_{char} as a time scale and ρv_{char}^2 as a pressure scale. The dimensionless temperature is defined as $T^* = (T - T_\infty)/(T_S - T_\infty)$. In what follows, we omit the "*" in the notation of the non-dimensionalized quantities, thus $\mathbf{v}$, p and T stand for non-dimensionalized velocity, pressure and temperature, respectively. The dimensionless equations become, for the mixed convection,

$$\nabla \cdot \mathbf{v} = 0 \tag{1}$$

$$\frac{\partial \mathbf{v}}{\partial t} + (\mathbf{v} \cdot \nabla)\mathbf{v} = -\nabla p + \frac{1}{Re}\nabla^2 \mathbf{v} + \frac{Gr}{Re^2} T\mathbf{i} \tag{2}$$

$$\frac{\partial T}{\partial t} + (\mathbf{v} \cdot \nabla)T = \frac{1}{Re.Pr}\nabla^2 T. \tag{3}$$

where $\mathbf{i} = -\mathbf{g}/|\mathbf{g}|$ stands for the upward oriented unit vertical vector. The non-dimensionalization reduces the parameters to three non-dimensional numbers – Reynolds number (Re), Grashof number (Gr) and Prandtl number (Pr) defined as follows:

$$Re = \frac{v_{\text{char}} d}{\nu}, \quad Gr = \frac{\beta g(T_S - T_\infty)d^3}{\nu^2}, \quad Pr = \frac{\nu}{\kappa}. \tag{4}$$

The combination of the first two parameters gives the Richardson number ($Ri = Gr/Re^2$), a non-dimensionalized parameter comparing the effect of the natural convection to that of the forced one.

In the case of free convection, the use of the velocity scale $v_{\text{char}} = \sqrt{\beta g(T_S - T_\infty)d}$ yields $Re = \sqrt{Gr}$ in Eqs. (2 and 3).

The boundary conditions are the no-slip boundary condition and uniform unit temperature at the sphere surface S

$$\mathbf{v}|_S = 0, \quad T|_S = 1. \tag{5}$$

At infinity, the velocity tends to the free stream velocity $\mathbf{v}_\infty$ or to zero, for assisting flow or free convection, respectively, and the temperature is assumed to be zero:

$$\mathbf{v}|_\infty = \mathbf{v}_\infty, \quad T|_\infty = 0. \tag{6}$$

3. Numerical method

The infinite domain is simulated by a cylindrical computational domain, the section in the radial–axial plane of which is represented in Fig. 2. The domain axis is oriented along the x-axis of Fig. 1. To simulate an infinite domain, the size of the domain was thoroughly tested in all the simulated regimes and adapted so that its extension upstream, downstream and sidewise brought no significant changes to the flow and, namely, no longer changed the computed drag coefficient and Nusselt number, as well as the regular instability threshold (see Appendix A for more details on the testing). A good choice of boundary conditions at the outer boundaries helps to reach the domain independence. The boundary conditions in most simulations consisted in setting the Dirichlet boundary condition $\mathbf{v} = \mathbf{v}_\infty$ and $T = 0$ at the inflow cylinder face and at its outer perimeter. For most simulations the Reynolds numbers were relatively high (up to on the order of 1500). In such conditions, the combined wake/plume extends extremely far downstream. The Neumann condition $\frac{\partial \mathbf{v}}{\partial \mathbf{n}} = 0$ and $\frac{\partial T}{\partial n} = 0$, imposed in a weak sense, allows to keep the outflow boundary at a reasonable distance without affecting the solved flow [28]. This condition appears to present no reflections in the transitional regimes and the flow remains unaffected by the position of the outflow boundary of the computational domain. Indeed, as can be seen from the results of numerical testing presented in Appendix A, the position of the outflow boundary is the numerical parameter that affects the least the obtained results. It is also to be noted that the chosen Dirichlet and Neumann boundary conditions fully determine the velocity field. As a consequence, no boundary conditions need to be specified on the pressure (see e.g. [38, p. 21], for the Dirichlet case).

The method of spatial discretization is described in detail in [28] or [34]. It is based on the spectral element decomposition (see [39,40]) in the radial–axial plane combined with a spectral azimuthal decomposition to accommodate 3D flows. The implementation of the azimuthal decomposition enables, in a very straightforward way and at relatively low computing costs, the linear stability analysis of the flow with respect to axisymmetry breaking perturbations [33]. For the purpose of investigation of convective flows, the solver described in Ref. [28] has been completed by adding the energy equation. Moreover, the significantly higher Reynolds numbers of the present study imposed heavier requirements on the solution accuracy. For this reason, the projection method of the pressure–velocity coupling has been reformulated to yield an orthogonal projector within machine accuracy and a direct pressure solver has been implemented. This resulted both in an enhanced accuracy and in very significant gains of CPU time. This was important not only because of the high resolution needed but also because of the fact that the

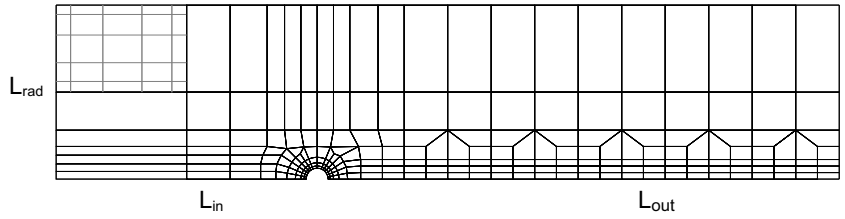

Fig. 2. Example of a computational domain of 230 elements with collocation points of the upper-left element.

parametric study involved many points in the parameter space. The investigation of the instability thresholds is, itself, very sensitive to the space and time resolution and significant amount of additional accuracy testing was necessary to avoid spurious instabilities. This resulted in many more runs. Moreover, as compared to the unheated sphere, the linearized eigenvalue problem relative to the thermal flow appears to present several almost zero eigenvalues which makes it significantly more time consuming to isolate the least stable or the most unstable one.

The mentioned discretization testing focused on the parameters specified in Table 1. The domain size parameters have already been discussed above. The break up into spectral elements allows us to optimize the computational effort depending on the length scales of the computed flow structures. Within each spectral element the same number of collocation points of the pseudo-spectral Gauss–Lobatto–Legendre polynomial approximation is used. The variation of the number of collocation points (last column of Table 1) controls the overall accuracy. For more details on the results of testing refer to Appendix A.

4. Free convection

Although not the main focus of the paper, the free convection, with only two parameters, a Prandtl number mostly considered to be that of the air and a great number of available, both experimental and numerical results, is an important test case. In agreement with other numerical simulations, the present tests are axisymmetric which is physically reasonable in the considered interval of Grashof numbers ranging from 10^{-4} to 10^{4}. Our results are compared to that of [7–9] in terms of drag coefficient and Nusselt number. Fig. 3a represents the drag coefficient defined as

$$C_{\mathrm{D}}^{\mathrm{Dud}} = \frac{F_{\mathrm{D}}}{\rho v^2}, \tag{7}$$

where F_{D} stands for the drag, as a function of Grashof number. Dudek et al. and Geoola and Cornish use the above definition of the drag coefficient, Jia and Gogos define the drag coefficient as

$$C_{\mathrm{D}}^{\mathrm{Jia}} = \frac{F_{\mathrm{D}}}{\frac{1}{2}\rho v_{\mathrm{char}}^2 \frac{\pi d^2}{4}}, \tag{8}$$

which relates the two drag coefficients as follows:

$$C_{\mathrm{D}}^{\mathrm{Dud}} = C_{\mathrm{D}}^{\mathrm{Jia}} \frac{\pi Gr}{8}. \tag{9}$$

For low Grashof numbers ($\leqslant 10$) the dispersion of the values is quite significant and may be due to the sensitivity of the results to the domain size. For values of $Gr \geqslant 10$ we obtain a perfect agreement with the results of Jia and Gogos. Those of Geoola and Cornish seem to underestimate the drag coefficient for low Gr but agree well with those of Jia and Gogos at $Gr = 10^3$.

A very important characteristic of the flow is the Nusselt number, characterizing the efficiency of the convection. The Nusselt number is defined as the ratio of the total heat flux to the purely conductive one. For a heated sphere in an infinite medium, the conductive heat flux is

$$\dot{Q}_{\mathrm{cond,th}} = 2\pi\lambda(T_S - T_\infty)d. \tag{10}$$

However, most bibliographic results use a Nusselt number defined as

$$Nu = \frac{\alpha d}{\lambda} = \frac{\dot{Q}}{\pi\lambda(T_S - T_\infty)d} = 2\frac{\dot{Q}}{\dot{Q}_{\mathrm{cond,th}}}. \tag{11}$$

We retain the factor 2 to facilitate the comparisons. Let us note that, in view of the finite size of the numerical domain,

Table 1
Upstream (L_{in}/d), downstream (L_{out}/d) and sidewise (L_{rad}/d) length of the computational domain, number of elements in the mesh (NE) and number of collocation points per element direction (NP) as a function of Re

Re	L_{in}/d	L_{out}/d	L_{rad}/d	NE	NP
0–99	50	60	52	442	6
100–199	30	35	28	281	7
200–399	12	25	8	169	8
400–999	12	25	8	169	10
>1000	12	24	8	230	12

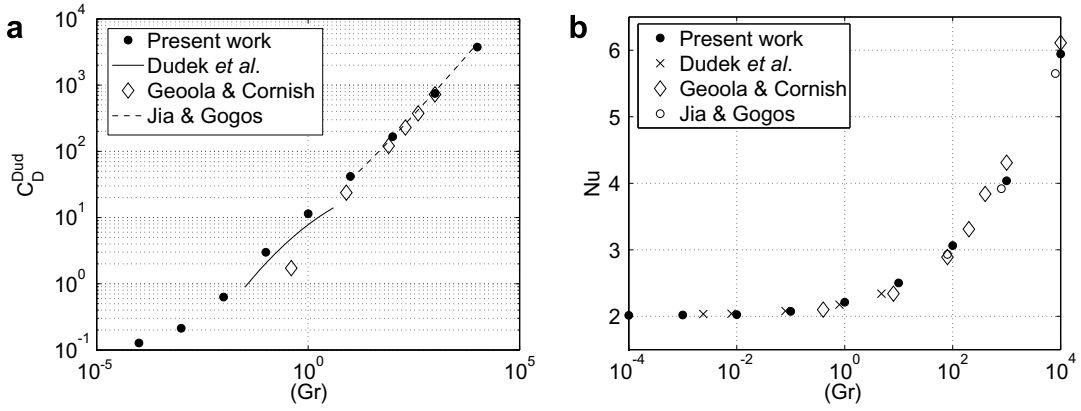

Fig. 3. (a) Drag coefficient and (b) overall Nusselt number: the case of pure free convection.

the numerical conductive heat flux $\dot{Q}_{cond}$ is different from the theoretical value $\dot{Q}_{cond,th}$ (e.g. for the small domain optimized for large Grashof numbers, we obtain, in the limit $Gr = 0$, $\dot{Q}_{cond} = 0.809\dot{Q}_{cond,th}$, while for the domain used for small Grashof numbers the same ratio is 0.985). To obtain an asymptotic Nu value equal to 2 for $Gr = 0$ and also to remain coherent with the fundamental definition, we use the numerical conductive heat flux instead of the theoretical one in the definition (11) for computations at very low Grashof numbers $Gr \leqslant 1$.

We compared again the results of our simulation to those of [7–9], see Fig. 3b. We obtain an excellent agreement with the results of Dudek et al. (available only for $Gr \leqslant 5$) and of Jia and Gogos (available for $Gr \geqslant 80$). Those of Geoola and Cornish are likely to underestimate the Nusselt number for small Gr and to overestimate it for high Gr.

In conclusion, namely the excellent agreement with the most recent and complete results of Jia and Gogos allows us to claim that our numerical method can be considered as reliable and accurate.

5. Mixed convection – axisymmetric assisting flow for $Pr = 0.72$

For wakes without buoyancy effects the flow separation has been recognized as an early precursor sign of the transition (e.g. [35]). In the case of a non-heated sphere, the flow separation results in a build up of recirculation very early, at a Reynolds number of 20, while the primary bifurcation sets in only at $Re = 212$ [37]. In the assisting flow past a sphere, the buoyancy effects accelerate the boundary layer and thus delay significantly its separation. Moreover, the build up of a convective plume tends to compensate the recirculation. The purpose of this section is to investigate the specificities of the combined shear and buoyancy effects with a special focus to the flow separation. This axisymmetric study is completed, in Section 7, by a stability investigation allowing to assess the relation between the loss of axisymmetry and the flow separation. The parameter plane is parameterized by the Reynolds and the Richardson numbers. This choice appears to be more convenient than that of the $Re - Gr$ parameterization because the results show that all analogy with the unheated sphere seems to be limited to Richardson numbers smaller than 0.7. As a result, a parameter domain of $0 \leqslant Ri \leqslant 0.7$ and $0 \leqslant Re \leqslant 1500$ is swept.

For low Richardson numbers ($Ri \leqslant 0.4$), the recirculation sets in on the flow axis downstream of the sphere in the same way as for an unheated sphere. The critical Reynolds number in such a case will be denoted Re_c. In contrast, for Richardson numbers $0.4 < Ri \leqslant 0.7$, we observe first a boundary layer separation off the flow axis at a Reynolds number denoted Re_s. This separation grows and generates a recirculation on the axis only later on at $Re_r > Re_s$. For $Re < Re_s$ (or $Re < Re_c$) and $Re > Re_c$ (or $Re > Re_r$) we observe no qualitative changes of the flow aspect compared to the unheated sphere, because for $Re < Re_s$ (or $Re < Re_c$) the flow is completely attached to the sphere surface (Fig. 4a) and for $Re > Re_c$ or ($Re > Re_r$), the flow presents a single (growing) recirculation vortex (Fig. 4b), similar to that of a non-heated sphere wake at $Re > 20.82$. The main purpose was then to cover the interval $[Re_s, Re_r]$.

5.1. Two different scenarios of the onset of flow recirculation

As already noted, the simulations have shown two different scenarios of the onset of recirculation depending on the Richardson number value.

5.1.1. Onset of the recirculation directly at the flow axis

For small Richardson numbers ($0 \leqslant Ri \leqslant 0.4$), the scenario of the onset of flow recirculation is similar to that of a non-heated sphere, see for example [37]. It is characterized by the critical Reynolds number Re_c at which a recirculation appears downstream of the sphere (see Fig. 5a). The only difference between non-heated sphere and heated sphere is that the effect of free convection significantly increases the value of Re_c (see Table 2).

5.1.2. Boundary layer separation off the flow axis

For $Ri > 0.4$ we observe that the boundary layer starts to separate off the flow axis at $Re = Re_s$ (Fig. 5b). Depending on Ri, the separation angle Φ_d at the onset of the boundary layer separation, measured from the front stagnation point, varies from 168° at $Ri = 0.4$ to 130° (at $Ri = 0.7$). The vortex grows until it reaches the flow axis and ends up by forming a recirculation zone along the axis (Fig. 5c) at a higher Reynolds number $Re_r > Re_s$. This behavior is clearly due to the plume generated by the convection, which accelerates the flow along the axis. As the Richardson number increases, the separation torus has to

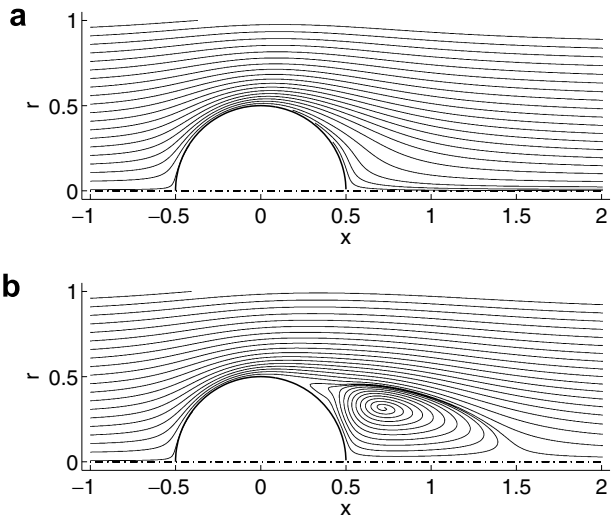

Fig. 4. Streamlines for the case of $Ri = 0.5$. (a) Attached flow at $Re = 200$ and (b) large recirculation zone downstream of the sphere at $Re = 600$.

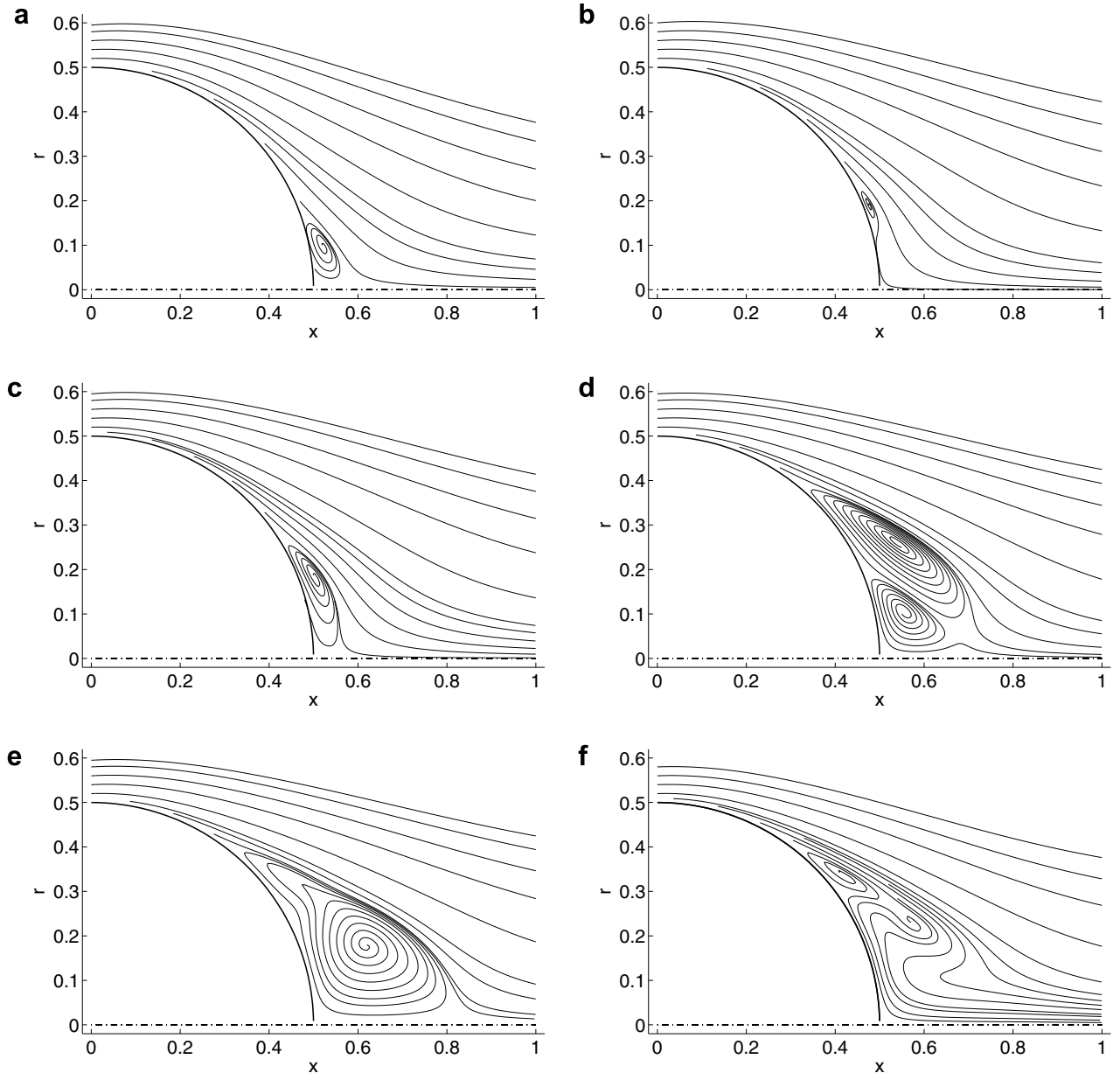

Fig. 5. Streamlines of observed flow patterns. (a) Recirculation downstream of the sphere at $Ri = 0.1$ and $Re = 25$ and (b) onset of the separation torus at $Ri = 0.425$ and $Re = 214$ (the respective detachment and reattachment angles are $\Phi_d = 153°$ and $\Phi_r = 166°$), (c) recirculation torus at the flow axis at $Ri = 0.425$ and $Re = 217.5$, (d) separation torus growing to the flow axis off the rear stagnation point at $Ri = 0.5$ and $Re = 380$, (e) recirculation at the flow axis downstream of the sphere at $Ri = 0.5$ and $Re = 450$, (f) flow separation at $Ri = 0.7$ and $Re = 1470$.

become stronger to be able to overcome the axial plume. It results in a large recirculation domain right at its onset (see Fig. 5d and e at $Ri = 0.5$). At $Ri \geqslant 0.57$ the recirculation at the flow axis is no longer reached in the laminar domain delimited in the next section. Instead, a secondary separation vortex appears immediately downstream of the first one (Fig. 5f). It is interesting to note that roughly the same limit of existence of the recirculation zone was found experimentally in [36] where the "suppression of the recirculation bubble" is reported at $Ri = 0.49$ (i.e. 0.7^2) independently of the Reynolds number.

The boundaries between the three domains of the three regimes, the attached flow, the separation off the flow axis and the recirculation at the axis have been explored in a detailed parametric study and are represented in Fig. 6. The representation is limited by the line beyond which the axisymmetric regime is no longer stable, which is discussed in Section 7. The figure sums up the results of 360 simulations not all of which are represented. Special attention has been paid to track the boundaries of the subdomains the points of which have been plotted in Fig. 10 to allow for the assessment of the plot accuracy.

Table 2
Thresholds for investigated regimes for $Pr = 0.72$ (left) and $Pr = 7$ (right) for varying Richardson numbers

Ri	Re_c (Re_s)	Re_r	Re_{crit}
Pr = 0.72			
0	20.82	–	212.0
0.001	21.02	–	212.4
0.01	22.75	–	215.9
0.1	30.10	–	257.1
0.2	47.20	–	321.0
0.3	84.50	–	397.7
0.4	153.4	157.4	514.7
0.5	314.9	415.0	679.4
0.55	424.1	720.0	786.9
0.6	553.1	–	1020
0.7	959.0	–	1471
Pr = 7			
0	20.82	–	212
0.1	31	–	240
0.2	58	–	287
0.25	96	101	324
0.3	161	240	383
0.35	261	460	516

5.2. Drag coefficient

Fig. 7a represents the drag coefficient defined as [37]

$$C_D = \frac{F_D}{\frac{1}{2}\rho v_\infty^2 \frac{\pi d^2}{4}}. \tag{12}$$

The figure represents curves of both constant Grashof and Richardson numbers obtained by interpolation from about 360 computed values. Hieber and Gebhart [11] suggest to split the value of the drag coefficient into two parts – a part due to the forced flow $C_D^{(c)}$ and a part due to the free-convective flow $C_D^{(f)}$ ($C_D = C_D^{(c)} + C_D^{(f)}$). The contribution due to the heating grows with Gr or, equivalently, Ri for a constant Re. This is the reason why for relatively small Grashof numbers ($Gr = 1$,10 and 100) the value of the drag coefficient is very close to that of an unheated sphere ($Gr = 0$) and why the curves $Gr = \text{const.}$ tend to be superposed for high Reynolds numbers. The change between the two flow regimes, described in Section 5.1, has no significant impact on the drag coefficient and the curves remain smooth. This allows to extend the law of Hieber and Gebhart [11]

$$C_D^{(f)} = \frac{12}{Re}[Ri + \lambda_1 RiRe + \lambda_2 Ri^2 + \lambda_3 RiRe^2 log(Re)], \tag{13}$$

proposed for small Re and Gr and $Ri = o(1)$, to the domain represented in Fig. 7a by Grashof numbers ranging from 0 to 5×10^5, or Richardson numbers from 0 to 2 and Reynolds numbers from 0 to 1000. We found very satisfactory agreement for fits both at each Gr constant (See Fig. 7b) and Ri constant. However, contrarily to Hieber and Gebhart, we found it impossible to obtain a satisfactory fully 2-D fit with coefficients λ_1, λ_2 and λ_3 independent of both Re and Gr (or Ri) in our much larger parameter domain.

5.3. Nusselt number and velocity profiles

Let's define the local Nusselt number as [6]

$$Nu_{loc} = -2\lambda\left(\frac{\partial T}{\partial n}\right)\frac{\pi d^2}{\dot{Q}_{cond}}, \tag{14}$$

where $\dot{Q}_{cond}$ is the purely conductive (numerical) heat flux. This definition yields the overall Nusselt number as the mean value [6]

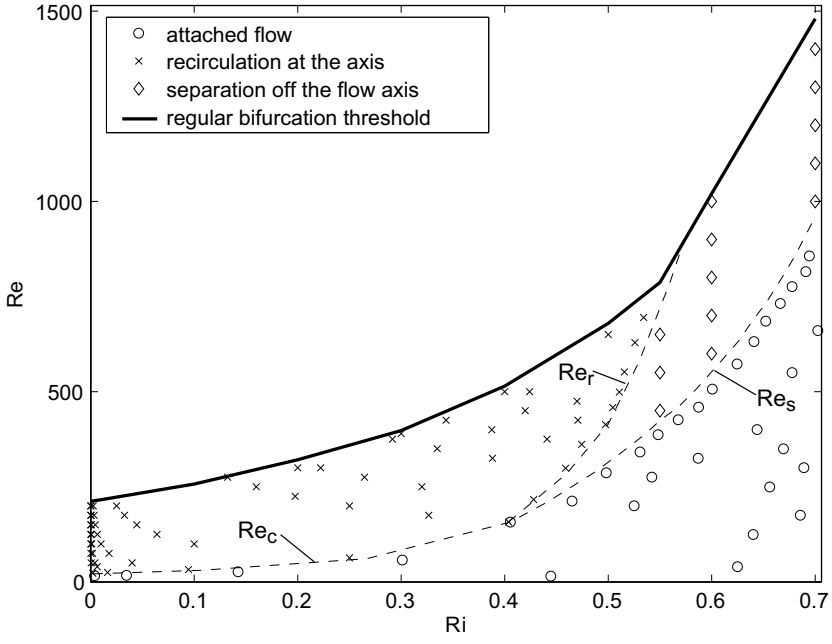

Fig. 6. Diagram of the investigated flow regimes.

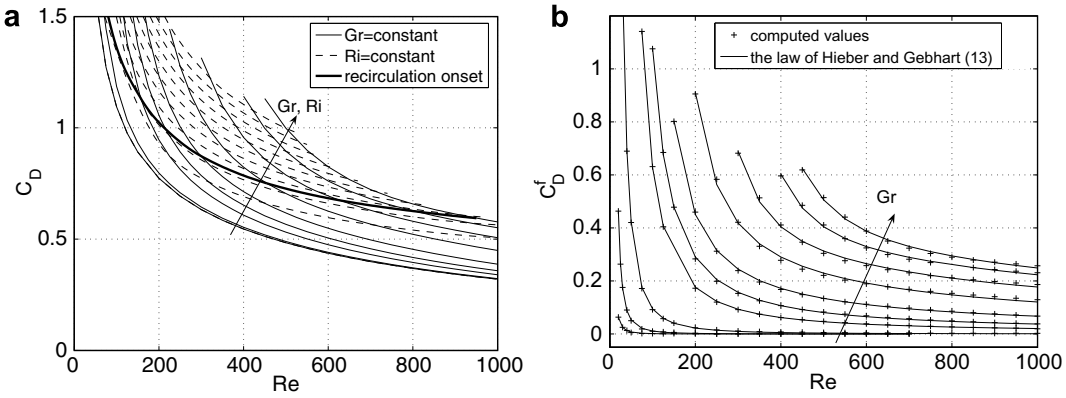

Fig. 7. The drag coefficient as a function of Reynolds, Grashof and Richardson numbers. (a) Curves representing the dependence of the total drag coefficient on Re for Grashof numbers $Gr = 0{,}10^3$, 10^4, 2×10^4, 4×10^4, 10^5, 2×10^5, 3.5×10^5, 5×10^5 (solid lines) and $Ri = 0$–2 incremented by 0.2 (dashed lines); the solid line for $Gr = 0$ and the dashed line for $Ri = 0$ are identical. The thick solid line connects the points where the large recirculation zone downstream of the sphere sets in. (b) Comparison of the computed contribution of the free convection to the drag coefficient to the law of Hieber and Gebhart (two more Gr values, 10 and 100, are added).

$$Nu = \frac{4}{\pi d^2} \int_S Nu_{\mathrm{loc}} \, \mathrm{d}S. \tag{15}$$

The local Nusselt number is shown in Fig. 8a for the case of $Ri = 0.5$ and four Reynolds numbers covering roughly the transition from the attached flow to the recirculation zone (see also Fig. 5d and e). On the upstream surface of the sphere ($0° \leqslant \theta \leqslant 100°$) the local Nusselt number increases with the Reynolds number. This is due to the velocity and temperature boundary layer getting thinner with growing Re. All four curves meet close to the point $\theta \approx 102°$ and from that point on an inverse effect sets in – the boundary layers thicken and the local Nusselt number decreases with increasing Re. The curves meet once again close to $\theta \approx 160°$. It can bee seen that the local heat exchange parameter is not significantly influenced by the flow separation except in the final regime with the large recirculation zone. The explanation is obvious from Fig. 9b where tangential velocity profiles at $Ri = 0.5$ and $Re = 400$ (a flow regime with a large separation torus touching the flow axis before the onset of the recirculation) are traced (Fig. 9a shows the flow pattern and the angles where the tangential velocities profiles were plotted). As can be seen from Fig. 9b, the velocity magnitude in the separated boundary layers is nearly 0 and the heat exchange is thus very limited. For a higher Re (>415), when the final recirculation downstream of the sphere sets in, the upstream flow along the flow axis is significant and thus the cold fluid from outside the sphere is mixed with the fluid near the sphere which results in a significantly increased local Nusselt number.

Fig. 8b shows the overall Nusselt number defined by Eq. (11) for selected Grashof numbers as a function of Reynolds number. In the same way as in Fig. 7a, curves at constant Gr and Ri are represented. The thick solid line connects the points where the final recirculation zone downstream of the sphere sets in. The enhancement of the heat transfer rate due to this recirculation zone becomes visible namely on the curves corresponding to high Grashof numbers ($Gr \geqslant 10^5$) as the change of the slopes of the curves.

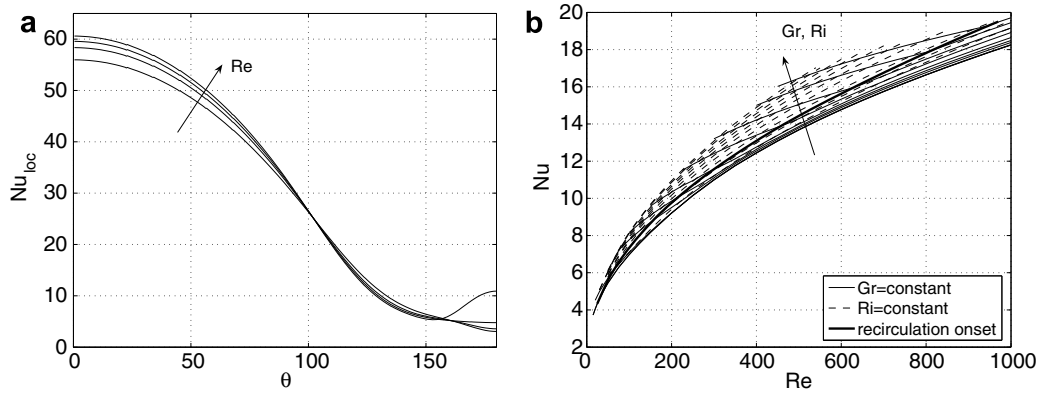

Fig. 8. (a) The local Nusselt number for $Ri = 0.5$ and $Re = 200$, 350, 400 and 450, (b) the overall Nusselt number represented by Nu vs. Re curves for constant Grashof and Richardson numbers (same values as in Fig. 7a). The thick solid line connects the points where the large recirculation zone downstream of the sphere sets in.

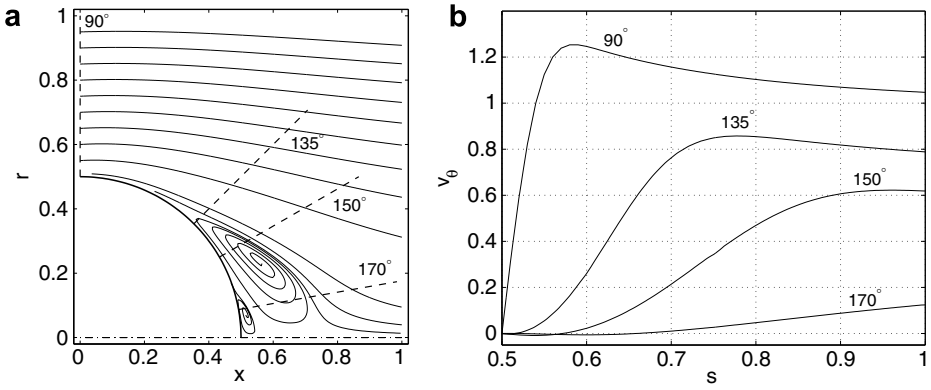

Fig. 9. (a) Flow aspect and angles at which the tangential velocities profiles are traced and (b) the tangential velocities profiles. $Ri = 0.5$ and $Re = 400$.

6. Mixed convection – assisting flow, effect of varying Prandtl number

In Section 5 we presented a detailed study for the case of $Pr = 0.72$. However, the study of the mixed convection would be incomplete if the effect of the Prandtl number were ignored. The aim of this section is not to provide a detailed study but to show how the results of Section 5 change when the Prandtl number increases or decreases.

6.1. Flow regimes

The three different flow regimes (attached flow, separation torus off the flow axis and the recirculation zone downstream of the sphere), studied in detail in previous section for $Pr = 0.72$, exist equally for $Pr = 7$ (see Fig. 10). Roughly speaking, the diagram appears to shrink within a smaller sub-domain of the two-parameter plane. The same trend is likely to exist for Prandtl numbers $Pr \leqslant 0.72$ and $Pr \geqslant 7$.

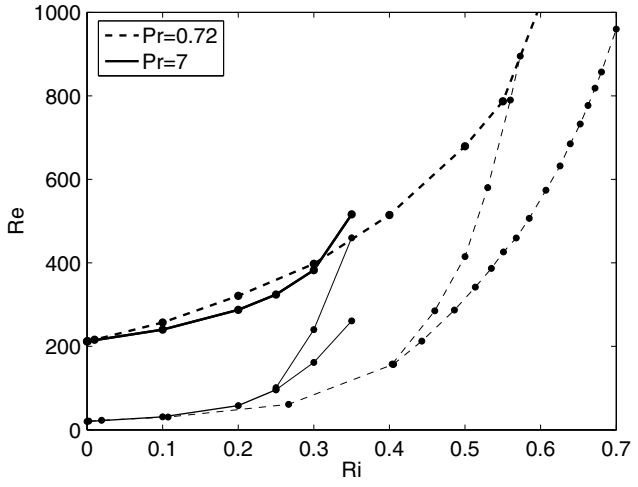

Fig. 10. Comparative phase diagram for $Pr = 0.72$ and 7. Dashed lines are lines from Fig. 6 ($Pr = 0.72$), solid lines represent $Pr = 7$. Thick, respectively solid and dashed lines, represent the regular instability threshold. Points determined accurately at the sub-domain boundaries are represented by solid dots.

6.2. Drag coefficient

Fig. 11 shows the drag coefficient for three Grashof numbers and two Prandtl numbers $Pr = 0.72$ and 7. There are no unexpected trends, for higher Pr the drag coefficient is smaller. The black points represent the recirculation onset (having no appreciable effect on the drag).

6.3. Nusselt number

Fig. 12a shows the overall Nusselt number for the same Grashof and Prandtl numbers as in the previous section. Naturally, the overall Nusselt number is higher for higher Prandtl number for a constant Gr because the conduction is reduced and there are higher temperature gradients at the sphere surface. The curves for $Pr = 7$ cross each other, which was not observed for $Pr = 0.72$. Due to the small thermal diffusivity, the convective heat exchange is more sensitive to the flow pattern. This is why the curves exhibit a significant change in derivative when the fluid starts to recirculate at the flow axis downstream of the sphere.

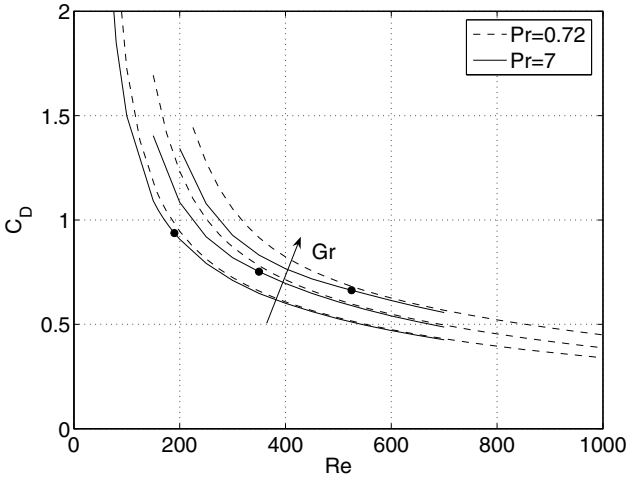

Fig. 11. Comparison of the drag coefficient for $Pr = 0.72$ and 7 and for $Gr = 10^4, 4 \times 10^4$ and 10^5. The points represent the onset of the large recirculation zone downstream of the sphere.

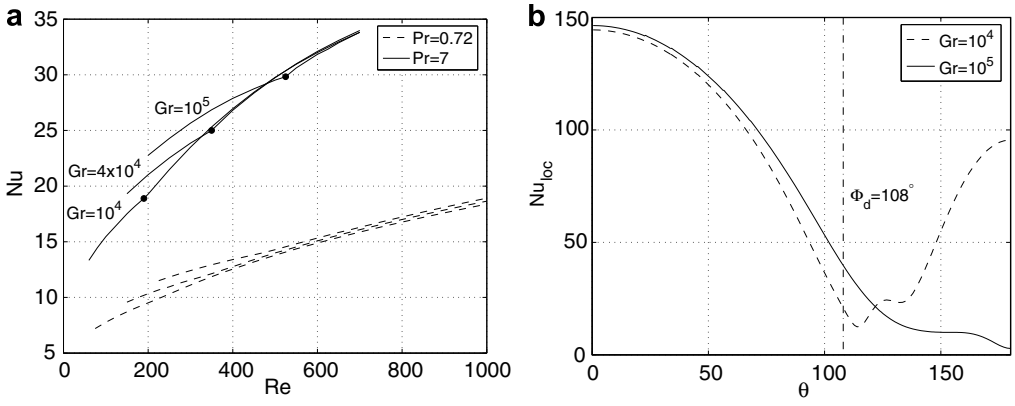

Fig. 12. (a) The overall Nusselt number for $Pr = 0.72$ and 7 and $Gr = 10^4$, 4×10^4 and 10^5, (b) the local Nusselt number for $Pr = 7$ and for two Grashof numbers ($Gr = 10^4$ and 10^5) at $Re = 480$. The points in (a) represent the onset of the large recirculation zone downstream of the sphere, the dash-dotted line in (b) represents the angle of flow separation Φ_d.

Thanks to that enhancement of heat exchange, the curve for a lower Grashof number crosses the curve of a higher Grashof number at a Reynolds number at which, in the former case, a large recirculation zone has set in and in the latter one the flow is still attached. This is visible in Fig. 12b where the local Nusselt numbers for both cases are plotted, the dash-dotted line representing the flow-detachment angle for the case of $Gr = 10^4$. Fig. 13 shows the corresponding flow patterns.

6.4. Extreme variation of the Prandtl number at constant Ri and Re

To study the effect of extreme Prandtl number values on the flow properties, we fixed the Richardson number at $Ri = 1$, the Reynolds number at $Re = 100$ and varied the Prandtl number from 0.1 to 100. Ri and Re were chosen so that the flow regime remains the same for all Prandtl numbers – the flow is attached.

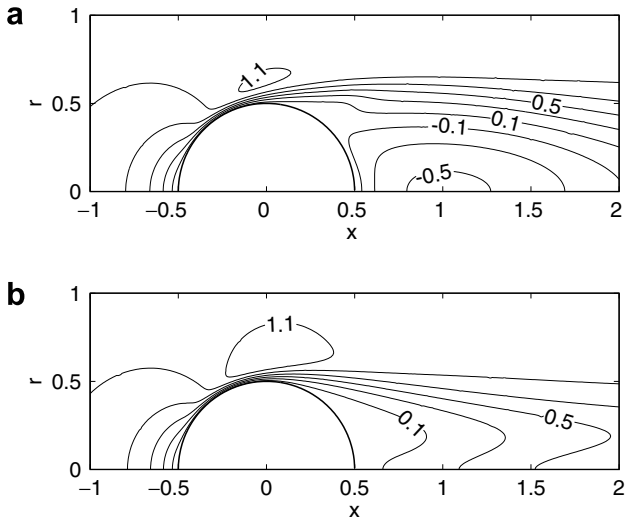

Fig. 13. The axial velocity isolines at $Re = 480$ and $Pr = 7$. (a) $Gr = 10^4$ ($Ri = 0.043$) and (b) $Gr = 10^5$ ($Ri = 0.43$).

Fig. 14a shows the drag coefficient as a function of Prandtl number. The drag coefficient is practically constant for $Pr \geqslant 20$. There is no net trend toward the value of 1.1 corresponding to the absence of heat transfer. This may be due to an insufficient resolution of the thermal boundary layer for very high Prandtl numbers.

The total heat flux tends asymptotically to zero like Pr^{-1}. More accurately, the $1/\dot{Q}$ vs. Pr dependence for $Pr \geqslant 40$ fits quite precisely to the linear law

$$\frac{1}{\dot{Q}} = 18.90 + 0.72Pr, \tag{16}$$

which means that the Nusselt number behaves like

$$Nu = \frac{Re}{\pi}\frac{Pr}{18.90 + 0.72Pr} \tag{17}$$

for large Prandtl numbers. Fig. 14b shows the overall Nusselt number as a function of Prandtl number, both the computed values and the law (17) are plotted.

To illustrate the influence of Prandtl number on the flow, the pressure at the sphere surface and flow axis (Fig. 15) as well as the temperature, axial velocity iso-values and the axial velocity profiles at several stations x (Fig. 16) for the two limit cases of $Pr = 0.1$ and 100 are plotted. As can be seen from the temperature plot, the greater Prandtl number the thinner the temperature boundary layer, which results in a reduced acceleration of the fluid due to the buoyancy. Also the buoyant plume is very thin for high Pr and is visible on the axial velocity profiles as a maximum at the flow axis.

7. Primary bifurcation and loss of axisymmetry for $Pr = 0.72$ and $Pr = 7$

The theory of axisymmetry breaking used in this section was exposed in detail in [28] (Section 2 of the cited paper). It has been namely shown that the axisymmetry of the base flow, equivalent to the fact that the linearized, fully three-dimensional, Navier–Stokes operator commutes with the

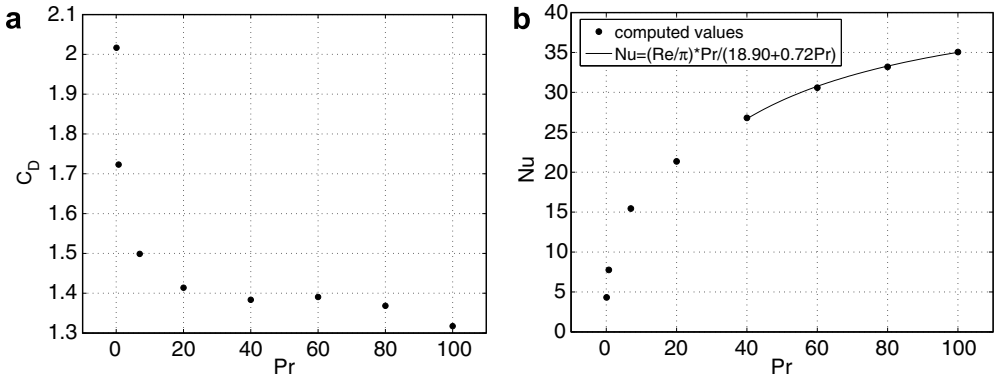

Fig. 14. (a) The drag coefficient and (b) the overall Nusselt number. $Ri = 1$ and $Re = 100$.

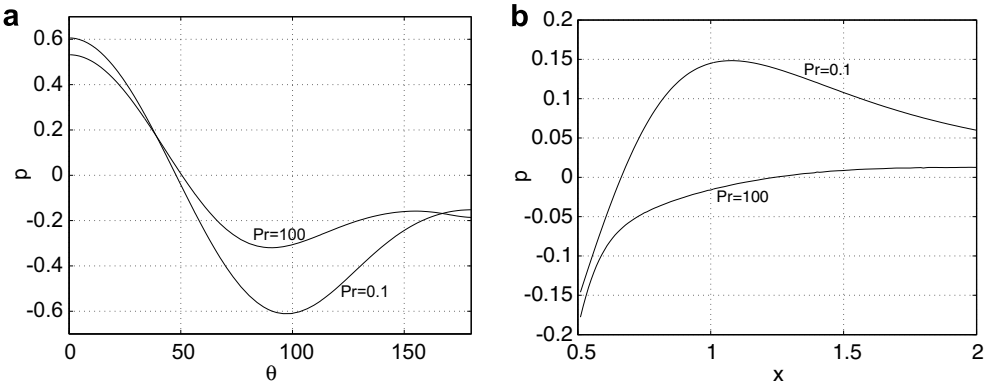

Fig. 15. The pressure distribution for two values of Prandtl number ($Pr = 0.1$ and $Pr = 100$) at $Ri = 1$ and $Re = 100$. (a) At the sphere surface and (b) at the flow axis downstream of the sphere.

operator of rotation $\partial/\partial\theta$ around the flow axis, implies that the linear stability problem can be split up by projection onto subspaces characterized by a specific azimuthal wavenumber m.

Our 3D Navier–Stokes solver based on the azimuthal Fourier expansion of the solution inspired by the non-linear theory, presented also in the same Section 2 of the cited paper [28], allows to solve directly the eigenvalue problem by truncating the azimuthal Fourier expansion to just one m-mode. This method has been applied to assess the stability of the steady axisymmetric solutions investigated in the preceding sections, i.e. at $Pr = 0.72$ and $Pr = 7$. The linear analysis of [28] carried out for an unheated sphere yields, in agreement with [25] and a series of other numerical and experimental papers cited therein, an unstable $m = 1$ mode associated to a real eigenvalue (regular bifurcation) showing that the first stage of axisymmetry breaking is steady and is characterized by a single period in the azimuthal direction.

A similar scenario has been confirmed up to $Ri = 0.7$ at $Pr = 0.72$ and up to $Ri = 0.35$ at $Pr = 7$. We solved the linearized eigenvalue problem for the least stable (most unstable) eigenvalue for varying Ri while focusing on the determination of the Reynolds numbers corresponding to the instability thresholds. The latter are obtained with a good accuracy by interpolation of amplification rates (eigenvalues) obtained from a pair of computations, one at a sub-critical and the other at a supercritical Reynolds number, both chosen close to the threshold. The mesh independence of computed eigenvalues has been tested, which resulted in further mesh refinement, in particular in the domain of higher Reynolds numbers. A sample of tests confirming the numerical convergence of the results is given in Appendix A.

The obtained regular instability thresholds are reported in Figs. 6 (thick solid line), 10 and in Table 2. The (axisymmetric and unstable) base flow at $Pr = 0.72$, $Ri = 0.5$ and $Re = 730$ is represented along with the streamwise velocity and temperature components of the unstable linear mode in Fig. 17. The effect of the mode is to deflect the central line of the wake/plume off the flow axis. In the same way as in the case of an unheated sphere of [28], the axisymmetry breaking bifurcation leads to a stable steady but non-axisymmetric flow. An example of such a flow is represented in Fig. 18 resulting from a fully 3D and thus fully non-linear simulation. (Note that the represented axial vorticity is zero for an axisymmetric flow.) The instability thresholds grow rapidly with increasing Richardson number. For $Pr = 0.72$ and at about $Ri \approx 0.7$ the curve leaves the investigated domain limited by a maximum Reynolds

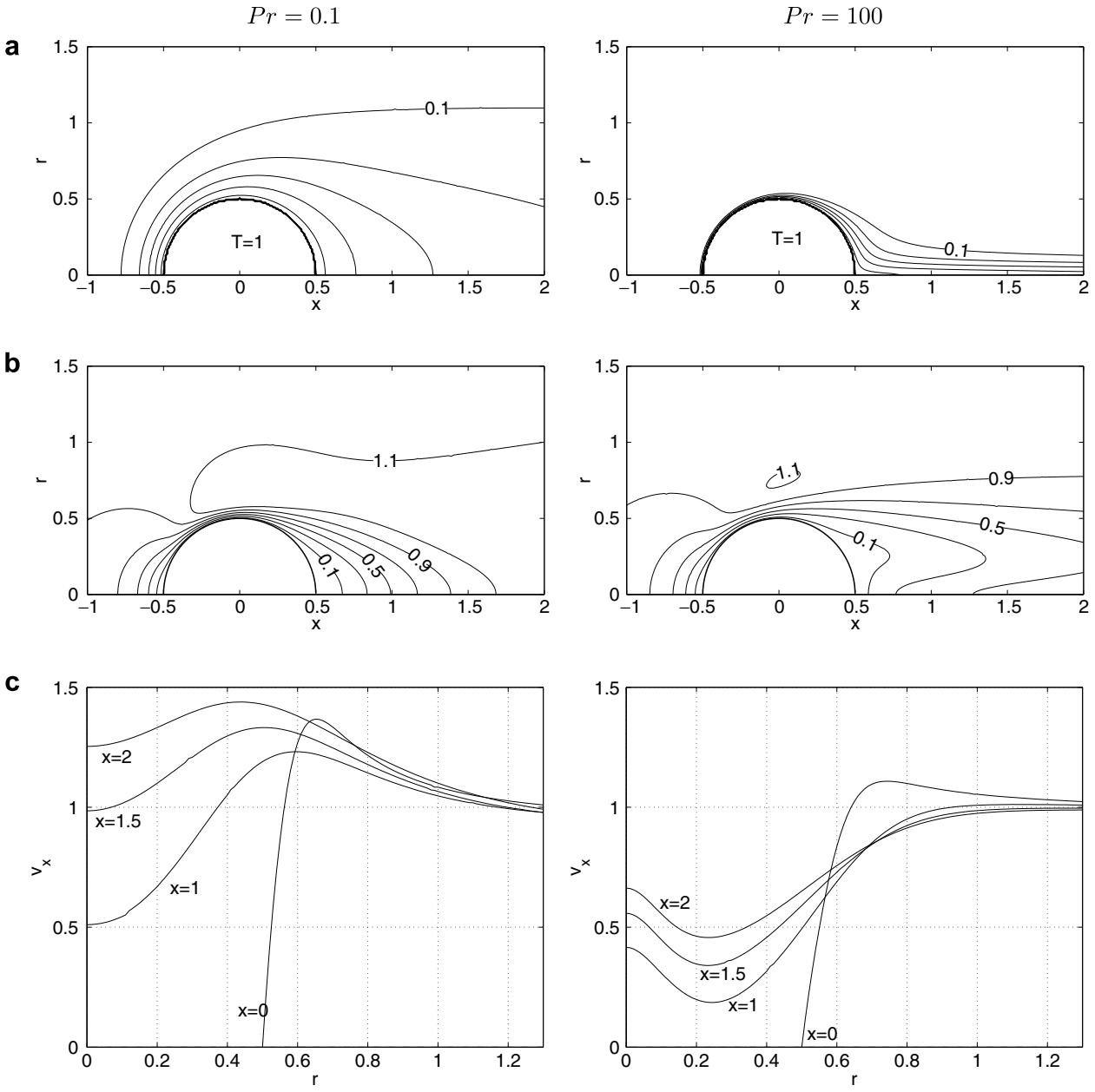

Fig. 16. (a) Temperature iso-values, (b) axial velocity iso-values, (c) axial velocity profiles at various stations x. $Ri = 1$, $Re = 100$, $Pr = 0.1$ (left) and $Pr = 100$ (right).

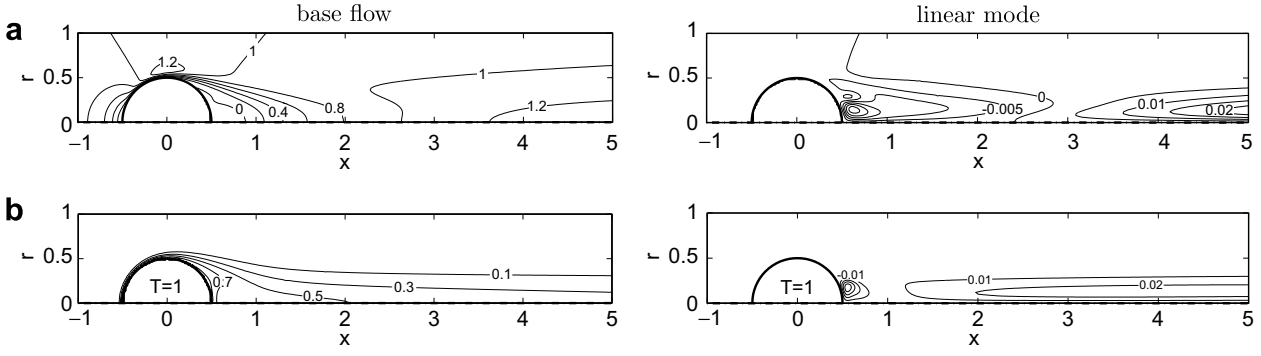

Fig. 17. (a) Axial velocity iso-values of the base flow (left) and of the linear mode (right), (b) temperature iso-values at $Ri = 0.5$, $Re = 730$. The linear mode is normalized so that the maximal value of axial velocity is 1 (this value lies at the domain outflow not represented in the figure).

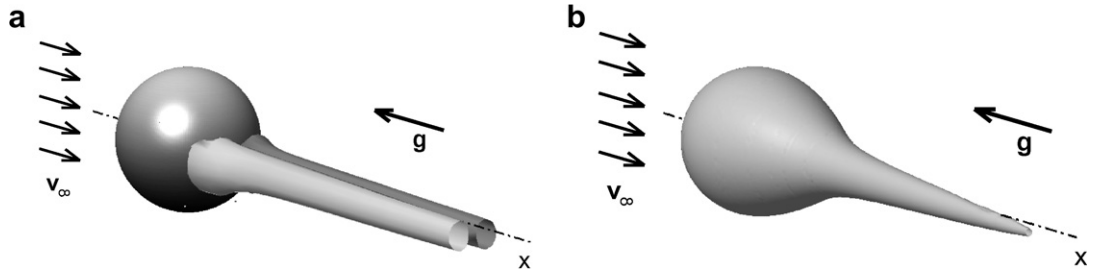

Fig. 18. (a) Iso-surfaces of axial vorticity at $\omega_x = \pm 0.15$ (the two vorticity threads are contra-rotating), (b) temperature iso-surface $T = 0.4$ at $Ri = 0.5$, $Re = 730$.

number of 1500 (at the limit of reasonable computing costs). It is interesting to note that the Prandtl number does not modify significantly the instability threshold within the investigated domain. At $Pr = 7$, the instability threshold lies below that obtained at $Pr = 0.72$, but both lines cross at $Ri \approx 0.3$. It can be seen that the computations presented in Sections 5 and 6 lie well within the stability domain of the axisymmetric flow at $Pr = 0.72$. For the same Pr and $Ri \geqslant 0.57$ it is clearly seen that the build up of the recirculation zone at the axis is no longer a necessary condition for the instability, nevertheless the flow separation sets in always well below the instability threshold and both curves, that relative to the flow separation and that of the instability threshold, remain parallel. This lets us to assume that the flow separation is likely to be a precursor sign of a regular bifurcation even at higher Richardson numbers unless another type of instability appears. Let us note that it might be a tricky and not necessarily physically relevant problem to try to track linear instabilities at higher Reynolds numbers. E.g., for cold axisymmetric jets there is no consensus whether they are linearly stable at all Reynolds numbers, nevertheless, there is a wide consensus going in the direction of a by-pass transition due to the receptivity to finite perturbations. This is likely to be the case for assisting flows at higher Richardson numbers at which the convective plume becomes dominant.

8. Conclusion

The scenario of the loss of axisymmetry of the mixed convection in the configuration of assisting flow past a heated sphere has been investigated fully for the Richardson number of $0 \leqslant Ri \leqslant 0.7$ and Reynolds numbers up to 1500 at $Pr = 0.72$ and for $0 \leqslant Ri \leqslant 0.35$ and $Re < 550$ at $Pr = 7$. It has been shown that the acceleration of the flow due to buoyancy considerably stabilizes the flow and pushes the onset of instabilities from $Re = 212$ for an unheated sphere to $Re = 1470$ at $Ri = 0.7$ and $Pr = 0.72$. At so high Richardson numbers the convective plume downstream of the sphere is so strong that it prevents the recirculation at the flow axis but the flow separation off the flow axis precedes the transition.

Within the domain of stability of the axisymmetric flow, we provide some useful results concerning the drag coefficient and the Nusselt number of the heated sphere. The analysis of the loss of axisymmetry puts the precision and reliability of the simulation under a particularly severe constraint. As a result, the drag and Nusselt number values obtained are likely to be very close to accurate. The proof that the flow remains stable to rather high Reynolds numbers gives credit of physical relevance also to the less detailed investigation of the effects of variable Prandtl numbers presented in Section 6. In view of this study, namely of the diagram in Fig. 10, the stabilizing trend for increasing Richardson number is to be expected to be steeper for $Pr > 0.72$ and slower for $Pr < 0.72$ as compared to that reported in Fig. 6 and Table 2, which might be explainable by high temperature gradients in the boundary layers for high Prandtl numbers.

Table 3
Test of the grid dependence on the number of collocation points per element direction NP (a), on L_{in}/d (b), L_{out}/d (c) and L_{rad}/d (d) (see Fig. 2 for the definition of the symbols)

Panel (a)				
NP	8	10	12	14
C_D	0.55424	0.55521	0.55546	0.55516
Nu	23.330	24.243	24.056	24.028
Re_{crit}	1479.3	1473.8	1470.6	1470.3
Panel (b)				
L_{in}/d	8	12	16	24
C_D	0.55564	0.55546	0.55536	0.55539
Nu	24.056	24.056	24.055	24.055
Re_{crit}	1469.1	1470.6	1472.6	1472.3
Panel (c)				
L_{out}/d	16	24	32	48
C_D	0.55539	0.55546	0.55539	0.55539
Nu	24.055	24.056	24.055	24.055
Re_{crit}	1472.4	1470.6	1471.9	1472.1
Panel (d)				
L_{rad}/d	4	8	12	20
C_D	0.55646	0.555546	0.55544	0.55554
Nu	24.063	24.056	24.055	24.056
Re_{crit}	1452.3	1470.6	1472.4	1471.4

The tests result from varying the parameters of the reference domain $L_{in}/d = 12$, $L_{out}/d = 24$, $L_{rad}/d = 8$ of 230 elements. Each time the parameter indicated on top left of the table is varied. The drag coefficient C_D and the Nusselt number Nu are computed at $Ri = 0.7$ and $Re = 1470$. The critical Reynolds numbers are evaluated by interpolation from amplification rates at Reynolds numbers lying below and above the instability threshold (in most cases between $Re = 1470$ and $Re = 1490$).

It may be reassuring to find that many axisymmetric results provided in the bibliography are likely to keep their physical relevance unless other mechanisms such as receptivity to finite perturbations are taken into account.

Appendix A. Tests of grid dependence

Table 3 presents a sample of results of numerical testing. Similar testing was carried out systematically at different flow regimes because each flow regime puts the discretization to a different constraint. At high Reynolds numbers, the resolution of the boundary layer is critical whereas at low Reynolds it is important to verify whether the domain extension is sufficient to eliminate spurious confinement by too closely placed boundaries. Here we choose the case of extreme Reynolds and Richardson values putting the mesh refinement under the most severe test. The values reported in the tables provide a clear idea of the accuracy of the domain mentioned on the last line of Table 1 and used for $Pr = 0.72$ and $Ri = 0.7$ close to $Re = 1500$. Similar accuracies are achieved for all other domains in their corresponding regimes.

References

[1] J.C. Lecordier, L. Hamma, P. Paranthoen, The control of vortex shedding behind heated circular cylinders at low Reynolds numbers, Exp. Fluids 10 (1991) 224–229.

[2] A.-B. Wang, Z. Trávníček, K.-C. Chia, On the relationship of effective Reynolds number and Strouhal number for the laminar vortex shedding of a heated circular cylinder, Phys. Fluids 12 (2000) 1401–1410.

[3] M.-H. Wu, A.-B. Wang, On the transitional wake behind a heated circular cylinder, Phys. Fluids 19 (2007), 084102–1–9.

[4] S.N. Brown, C.J. Simpson, Collision phenomena in free-convective flow over a sphere, J. Fluid Mech. 124 (1982) 123–137.

[5] V.N. Kurdyumov, A. Liñán, Free convection from a point source of heat, and heat transfer from spheres at small Grashof numbers, Int. J. Heat Mass Transfer 42 (1999) 3849–3860.

[6] F. Geoola, A.R.H. Cornish, Numerical solution of steady-state free convective heat transfer from a solid sphere, Int. J. Heat Mass Transfer 24 (1981) 1369–1379.

[7] F. Geoola, A.R.H. Cornish, Numerical simulation of free convective heat transfer from a sphere, Int. J. Heat Mass Transfer 25 (1982) 1677–1687.

[8] D.R. Dudek, T.H. Fletcher, J.P. Longwell, A.F. Sarofim, Natural convection induced drag forces on spheres at low Grashof numbers: comparison of theory with experiment, Int. J. Heat Mass Transfer 31 (1988) 863–873.

[9] H. Jia, G. Gogos, Laminar natural convection heat transfer from isothermal spheres, Int. J. Heat Mass Transfer 39 (1996) 1603–1615.

[10] A. Acrivos, On the combined effect of forced and free convection heat transfer in laminar boundary layer flows, Chem. Eng. Sci. 21 (1966) 343–352.

[11] C.A. Hieber, B. Gebhart, Mixed convection from a sphere at small Reynolds and Grashof numbers, J. Fluid Mech. 38 (1969) 137–159.

[12] L.S. Klyachko, Heat transfer between a gas and a spherical surface with the combined action of free and forced convection, J. Heat Transfer 85 (1963) 355–357.

[13] T. Yuge, Experiments on heat transfer from spheres including combined natural and forced convection, J. Heat Transfer C82 (1960) 214–220.

[14] D. Katoshevski, B. Zhao, G. Ziskind, E. Bar-Ziv, Experimental study of the drag force acting on a heated particle, J. Aerosol Sci. 32 (2001) 73–86.

[15] E. Bar-Ziv, B. Zhao, E. Mograbi, D. Katoshevski, G. Ziskind, Experimental validation of the Stokes law at nonisothermal conditions, Phys. Fluids 14 (2002) 2015–2018.

[16] G. Ziskind, B. Zhao, D. Katoshevski, E. Bar-Ziv, Experimental study of the forces associated with mixed convection from a heated sphere at small Reynolds and Grashof numbers. Part I: Cross-flow, Int. J. Heat Mass Transfer 44 (2001) 4381–4389.

[17] E. Mograbi, G. Ziskind, D. Katoshevski, E. Bar-Ziv, Experimental study of the forces associated with mixed convection from a heated sphere at small Reynolds and Grashof numbers. part II: assisting and opposing flows, Int. J. Heat Mass Transfer 45 (2002) 2423–2430.

[18] E. Mograbi, E. Bar-Ziv, Dynamics of a spherical particle in mixed convection flow field, J. Aerosol Sci. 36 (2005) 387–409.

[19] T.S. Chen, A. Mucoglu, Analysis of mixed forced and free convection about a sphere, Int. J. Heat Mass Transfer 20 (1977) 867–875.

[20] A. Mucoglu, T.S. Chen, Mixed convection about a sphere with uniform surface heat flux, J. Heat Transfer 100 (1978) 542–544.

[21] K.L. Wong, S.C. Lee, C.K. Chen, Finite element solution of laminar combined convection from a sphere, J. Heat Transfer 108 (1986) 860–865.

[22] H.D. Nguyen, S. Paik, J.N. Chung, Unsteady mixed convection heat transfer from a solid sphere: the conjugate problem, Int. J. Heat Mass Transfer 36 (1993) 4443–4453.

[23] R. Nazar, N. Amin, I. Pop, On the mixed convection boundary-layer flow about a solid sphere with constant surface temperature, The Arabian J. Sci. Eng. 27 (2002) 117–135.

[24] E. Mograbi, E. Bar-Ziv, On the mixed convection hydrodynamic force on a sphere, J. Aerosol Sci. 36 (2005) 1177–1181.

[25] R. Natarajan, A. Acrivos, The instability of the steady flow past spheres and disks, J. Fluid Mech. 254 (1993) 323–344.

[26] T.A. Johnson, V.C. Patel, Flow past a sphere up to a Reynolds number of 300, J. Fluid Mech. 378 (1999) 19–70.

[27] D. Ormières, M. Provansal, Transition to turbulence in the wake of a sphere, Phys. Rev. Lett. 83 (1999) 80–83.

[28] B. Ghidersa, J. Dušek, Breaking of axisymetry and onset of unsteadiness in the wake of a sphere, J. Fluid Mech. 423 (2000) 33–69.

[29] R. Mittal, A Fourier–Chebyshev spectral collocation method for simulating flow past spheres and spheroids, Int. J. Numer. Meth. Fluids 30 (1999) 921–937.

[30] J.H. Ferziger, M. Perić, Computational Methods for Fluid Dynamics, Springer, 1997.

[31] D.D. Gray, A. Giorgini, The validity of the Boussinesq approximation for liquids and gases, Int. J. Heat Mass Transfer 19 (1976) 545–551.

[32] M. Jenny, G. Bouchet, J. Dušek, Nonvertical ascension or fall of a free sphere in a Newtonian fluid, Phys. Fluids 15 (2003) L9–L12.

[33] M. Jenny, J. Dušek, G. Bouchet, Instabilities and transition of a sphere falling or ascending freely in a Newtonian fluid, J. Fluid Mech. 508 (2004) 201–239.

[34] M. Jenny, J. Dušek, Efficient numerical method for the direct numerical simulation of the flow past a single light moving spherical body in transitional regimes, J. Comput. Phys. 194 (2004) 215–232.

[35] X. Yang, A. Zebib, Absolute and convective instability of a cylinder wake, Phys. Fluids A 1 (1989) 689–696.

[36] N. Michaux-Leblond, M. Bélorgey, Near-wake behavior of a heated circular cylinder: viscosity-buoyancy duality, Exp. Thermal Fluid Sci. 15 (1997) 91–100.

[37] M. Mebarek, G. Bouchet, J. Dušek, Hydrodynamic forces acting on a rigid fixed sphere in early transitional regimes, Eur. J. Mech. B/Fluids 25 (2006) 321–336.

[38] R. Temam, Navier–Stokes Equations, North-Holland, 1977.

[39] A. Patera, A spectral element method for fluid dynamics: laminar flow in a channel expansion, J. Comput. Phys. 54 (3) (1984) 468–488.

[40] G.E. Karniadakis, Spectral element-Fourier methods for incompressible turbulent flows, Comput. Methods Appl. Mech. Eng. 80 (3) (1990) 367–380.